Article

Molecular-Frame Photoelectron Angular Distributions of CO in the Vicinity of Feshbach Resonances: An XCHEM Approach

Vicent J. Borràs, Jesús González-Vázquez, Luca Argenti, and Fernando Martín*

Read Online

ACCESS | Metrics & More | Article Recommendations

ABSTRACT: The advent of ultrashort XUV pulses is pushing for the development of accurate theoretical calculations to describe ionization of molecules in regions where electron correlation plays a significant role. Here, we present an extension of the XCHEM methodology to evaluate laboratory- and molecular-frame photoelectron angular distributions in the region where Feshbach resonances are expected to appear. The performance of the method is demonstrated in the CO molecule, for which information on Feshbach resonances is very scarce. We show that photoelectron angular distributions are dramatically affected by the presence of resonances, to the point that they can completely reverse the preferred electron emission direction observed in direct nonresonant photoionization. This is the consequence of significant changes in the electronic structure of the molecule when resonances decay, an effect that is mostly driven by electron correlation in the ionization continuum. The present methodology can thus be helpful for the interpretation of angularly resolved photoionization time delays in this and more complex molecules.
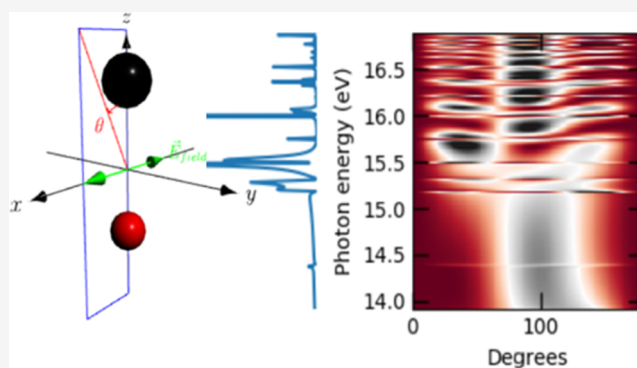
1. INTRODUCTION

The development of few-femtosecond and attosecond XUV pulses has opened the door to perform experiments that can access the electronic time scale in atoms and molecules. Due to their high energy, absorption of just one XUV photon is enough to ionize any of these systems. Therefore, a theoretical description of the interaction with XUV light sources requires the evaluation of the electronic continuum of atoms and molecules. In systems containing more than one electron, besides direct photoionization, where the incoming photon is absorbed by a single electron, other ionization processes involving several electrons are possible, e.g., excitation of Feshbach resonances followed by their Auger decay or ionization accompanied by the excitation of the parent ion leading to so-called satellite and shake-up lines in high-resolution photoelectron spectra recorded in third-generation synchrotron facilities.[1] Any realistic theoretical description of these processes must be able to describe electron correlation in the ionization continuum. Among the various photoionization observables, molecular-frame photoelectron angular distributions are particularly challenging, as these are extremely sensitive to tiny spatial differences in electron correlation.

Recent experimental efforts in attosecond science have been aimed at studying even more challenging observables, namely, the angular dependence of atomic[2,3] and molecular[4−6] ionization time delays of photoelectrons with kinetic energies of a few tens of eV. At these energies, the ionization continuum is usually brimming with Feshbach resonances, which, in the case of atomic targets, are known to have a strong influence in the measured photoionization time delays.[2,7,8] In the case of molecules, a complete angular information on photoionization delays can only be obtained by determining the orientation of the molecule at the instant of ionization, i.e., by measuring molecular-frame photoelectron angular distributions (MFPADs). This is nowadays feasible by combining the techniques of attosecond science with multicoincidence detection methods, such as cold target recoil ion momentum spectroscopy (COLTRIMS).[9] Although this is a well-established procedure in experiments that employ synchrotron radiation, its implementation with attosecond light sources is quite demanding due to the low photon flux provided by these sources in comparison with synchrotrons.[4,10,11] In the case of the hydrogen molecule, theory has shown that many of the features observed in the photoionization time delays[10] are due to the presence of autoionizing states. One can expect that this will also be the case in more complex molecules, as these states
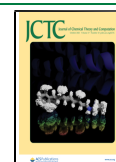
are quite apparent in the corresponding photoionization spectra recorded at synchrotrons (see, e.g., refs [12−18]). Recent measurements of angularly resolved photoionization delays in CO[4] have mainly focused on the nonresonant features of ionization, for which electron correlation effects are not so crucial. However, a complete understanding of photoionization delays within few-eV from the photoionization threshold of this molecule requires accounting for the CO autoionizing states.

These experimental efforts have spurred the development of theoretical approaches that can accurately account for electron correlation in the ionization continuum of molecules. Such methods are already well established in atoms (see, e.g., refs [19], [20]). In molecules, the multicenter nature of the potential makes the situation much more challenging. Quantum Chemistry packages are extremely successful and efficient in the description of electronic bound states using multicenter Gaussian functions. However, due to the rapid exponential decay of Gaussian functions, they have been shown to be inappropriate for the description of electronic continuum states. Thus, most existing methods for molecular ionization complement standard polycentric Gaussian functions with other basis functions that allow for an accurate description of the oscillatory behavior of the electronic continuum wave function at long distances. Among these methods, one can cite the UK Molecular R-Matrix method,[21,22] tRecX,[23,24] the multichannel Schwinger configuration interaction method (MCSCI),[25−28] the complex Kohn method,[29−33] and the XCHEM approach.[34,35]

The XCHEM method has been designed to interface standard Quantum Chemistry packages to provide an accurate description of electron correlation and exchange at a level comparable to that provided by complete or restricted active-space self-consistent field (CASSCF or RASSCF) methods for bound states, and hence, it is ideally suited to describe resonances in the electronic continuum.[12,15] In particular, XCHEM makes use of a hybrid Gaussian-B-Spline basis (GABS),[34] in which the usual polycentric Gaussian basis functions supplied by Quantum Chemistry packages are supplemented by monocentric Gaussian and B-spline functions. The correct asymptotic boundary conditions are imposed by solving the scattering equations within a close-coupling (CC) approach. XCHEM has been shown to provide accurate photoionization spectra in the resonance regions of He,[35] Ne,[36] N$_2$,[12,15] and O$_2$.[18]

In this paper, we present an extension of the XCHEM code that provides accurate laboratory- and molecular-frame photo-electron angular distributions in the region where Feshbach resonances are expected to appear. We have applied it to the CO molecule for which information about Feshbach resonances or studies on how these resonances manifest themselves are scarce.[17] We reveal the presence of many of these resonances close to $X^2\Sigma^+$ and $A^2\Pi$ ionization thresholds and a strong variation of the calculated MFPADs with photoelectron energy, which may have a drastic influence on photoionization time delays in this energy region. The origin of these variations is ascribed to the abrupt change in the electron density due to electron correlation, which can reverse the preferred electron emission direction in comparison to what one would expect if the electron was directly ejected.

The paper is organized as follows. In Section 2, we present the basic equations used in our implementation of electron angular distributions. In Section 3, we describe the computa-tional methods, and in Section 4, our results for the case of the CO molecule are presented. We discuss the results in Section 5 and summarize the most important conclusions of our work in Section 6. Atomic units are used throughout unless otherwise stated.

2. THEORY

The plane-wave scattering state $|\Psi^-_{\alpha E \hat{k}\sigma}\rangle$ for a molecular ion α coupled to an electron with defined energy E, spin projection σ, and electron emission direction $\hat{k}$, fulfilling incoming boundary conditions, is asymptotically

$$|\Psi^-_{\alpha E \hat{k}\sigma}\rangle = \sum_{lm} i^{l-1} Y^*_{lm}(\hat{k}) e^{-i\sigma_l(k)} \sum_{S\Sigma} \langle S_\alpha, \tfrac{1}{2}, S|\Sigma_\alpha, \sigma\rangle$$
$$\sqrt{N} \hat{\mathcal{A}} \Phi_\alpha(x_1, ..., x_{N-1}, \zeta_N) Y_{lm}(\hat{r}_N) \mathcal{W}^+_{l, E-E_\alpha}(r_N)$$
$$+ \text{incoming} \qquad (1)$$

where $k = \sqrt{2(E - E_\alpha)}$, N is the total number of electrons, $\sigma_l(k)$ is the Coulomb phase, $\langle a, b, c|\alpha, \beta\rangle$ is a Clebsch−Gordan coefficient, $\hat{\mathcal{A}} \equiv (N!)^{-1} \sum_{\mathcal{P} \in \mathcal{S}_N} (-1)^p \mathcal{P}$ is the idempotent antisymmetrizer, $\Phi_\alpha(x_1, ..., x_{N-1}, \zeta_N)$ is the parent-ion function coupled to the spin function of the photoelectron to give a total spin and spin projection S and Σ, respectively, ζ_N is the spin variable of the last electron, $x_i = (\vec{r}_i, \zeta_i)$ are the spatial and spin coordinates of ion electrons, $Y_{lm}(\hat{\Omega})$ is a spherical harmonic, $\mathcal{W}_{l,E}(r)$ is the outgoing component of a regular Coulomb function normalized to $\delta(E - E')$, and "incoming" refers to the residual purely incoming components in all of the open channels. The plane-wave scattering state $|\Psi^-_{\alpha E \hat{k}\sigma}\rangle$ can be expressed in terms of spherical scattering states $|\Psi^-_{\alpha lmE}\rangle$, in which the outgoing photoelectron has a well-defined orbital angular momentum, as

$$|\Psi^-_{\alpha E \hat{k}\sigma}\rangle = \sum_{lm} i^{l-1} Y^*_{lm}(\hat{k}) e^{-i\sigma_l(k)} \sum_{S\Sigma} \langle S_\alpha, \tfrac{1}{2}, S|\Sigma_\alpha, \sigma\rangle |\Psi^-_{\alpha lmE}\rangle$$
$$(2)$$

The XCHEM code computes the scattering states in which the outgoing channel has the angular distribution of symmetry-adapted spherical harmonics X_{lm} instead of the ordinary spherical harmonics Y_{lm},

$$X_{l0} = Y_{l0} \qquad (3)$$

$$X_{lm} = \frac{1}{\sqrt{2}}(Y_{lm} + (-1)^m Y_{l-m}), \quad m > 0 \qquad (4)$$

$$X_{l-m} = \frac{1}{\sqrt{2}\,i}(Y_{lm} - (-1)^m Y_{l-m}), \quad m > 0 \qquad (5)$$

Conversely, we can express Y_{lm} in terms of X_{lm} as

$$Y_{lm} = \frac{a_m}{\sqrt{2}}(X_{lm} + ib_m X_{l-m}) \qquad (6)$$

where $a_m = 1$, if $m > 0$; $a_0 = \sqrt{2}$; $a_m = -i(-1)^m$, if $m < 0$; and $b_m = 1 - \delta_{m0}$.

The plane-wave scattering states, therefore, can be written in terms of the symmetry-adapted spherical waves $|\Psi^-_{aXlmE}\rangle$ as

$$|\Psi^-_{\alpha E \hat{k} \sigma}\rangle = \sum_{lm} i^{l-1} Y^*_{lm}(\hat{k}) e^{-i\sigma_l(k)} \sum_{S\Sigma} \langle S_\alpha, \tfrac{1}{2}, S|\Sigma_\alpha, \sigma\rangle$$
$$\frac{a_m}{\sqrt{2}}(|\Psi^-_{\alpha XlmE}\rangle + ib_m|\Psi^-_{\alpha Xl-mE}\rangle) \tag{7}$$

Finally, the spherical components of the electronic dipole operator are defined from the Cartesian components used in XCHEM as

$$d_1 = -\frac{d_x + id_y}{\sqrt{2}} \tag{8}$$

$$d_0 = d_z \tag{9}$$

$$d_{-1} = \frac{d_x - id_y}{\sqrt{2}} \tag{10}$$

A useful general expression of these relations is

$$d_p = \left(1 - |p| + \frac{1}{\sqrt{2}}|p|\right)[-pd_x - i|p|d_y + (1 - |p|)d_z] \tag{11}$$

2.1. Molecular-Frame Photoelectron Angular Distributions. The partial molecular-frame photoelectron angular distribution (MFPAD) $\frac{dP_\alpha}{dEd\Omega}$ is given by

$$\frac{dP_\alpha}{dEd\hat{k}} = \sum_{\sigma\Sigma_\alpha} |\langle\Psi^-_{\alpha E\hat{k}\sigma}|\Psi\rangle|^2 \tag{12}$$

Let $A_{\alpha lmE} = \langle\Psi^-_{\alpha XlmE}|\Psi\rangle$ be the partial photoelectron amplitude of the wave packet Ψ that results from the interaction of the molecule with an external field. In the case of intense pulsed fields, Ψ may be computed by solving the TDSE numerically, whereas in the case of one-photon transition in stationary conditions, Ψ is simply proportional to the action of the dipole operator on the initial bound state of the molecule. Using eq 7, we can then rewrite the MFPAD as

$$\frac{dP_\alpha}{dEd\hat{k}} = (2S_0 + 1) \sum_{j\mu} Y_{j\mu}(\hat{k})B_{j\mu} \tag{13}$$

where

$$B_{j\mu} = \sum_{ll'} \frac{\Pi_{jl'}}{\sqrt{4\pi}\Pi_l} i^{l'-l} e^{i(\sigma_l - \sigma_{l'})}\langle j, l', l|0, 0\rangle \sum_{mm'} \langle j, l', l|\mu, m'\rangle$$
$$\frac{a^*_m a_{m'}}{2}[A_{\alpha lmE} - ib_m A_{\alpha l-mE}][A^*_{\alpha l'm'E} + ib_{m'}A^*_{\alpha l'-m'E}] \tag{14}$$

$\Pi_{ab\cdots} = \sqrt{(2a+1)(2b+1)\cdots}$, and we have used the well-known formula for the integral of the triple product of spherical harmonics, $\langle Y_{a\alpha}|Y_{b\beta}Y_{c\gamma}\rangle = \frac{\Pi_{bc}}{\sqrt{4\pi}\Pi_a} C^{a0}_{c0,b0} C^{a\alpha}_{c\gamma,b\beta}$.

2.2. β Parameter. Within the dipole approximation, the one-photon ionization of randomly oriented molecules gives rise to a photoelectron angular distribution that depends on just a single real number, known as β asymmetry parameter.[37] The general expression that defines this parameter (β) is

$$\frac{d\sigma_{\mu'}}{dEd\Omega} = \frac{\sigma_{\mu'}}{4\pi}[1 + \beta\mathcal{P}_2(\cos\theta)] \tag{15}$$

where μ' refers to a photon polarized in the z direction of the laboratory frame, $\sigma_{\mu'}$ is the total cross section, $\mathcal{P}_2$ is the well-

known Legendre polynomial and θ is the angle between the laser polarization and photoelectron.

To derive the correct expression of β for the XCHEM code, we start from the expression of the cross section in the length gauge

$$\frac{d\sigma_{\mu'}}{dEd\Omega} = \sum_{\sigma\Sigma_\alpha} \frac{\omega'}{2c} \int d\hat{R}|\langle\Psi_0|\hat{d}_{\mu'}|\Psi^-_{\alpha E\hat{k}\sigma}\rangle|^2 \tag{16}$$

where Ψ_0 is the ground state wave function, $\hat{d}_{\mu'}$ is the dipole transition operator in the laboratory frame, and $|\Psi^-_{\alpha E\hat{k}\sigma}\rangle$ is the plane-wave scattering state defined before, in which the direction of the photoelectron ($\hat{k}$) is referred to the molecular frame. Now, defining

$$|\Psi^-_{\alpha E\hat{k}\sigma}\rangle = \sum_{lm} Y^*_{lm}(\hat{k}) \sum_{S\Sigma} C^{S\Sigma}_{S_\alpha\Sigma_\alpha,1/2\sigma}|\Psi^-_{\alpha\sigma lmE}\rangle \tag{17}$$

and making use of Wigner rotation matrices to transform the dipole transition operator and the spherical harmonics to the molecular and laboratory frame, respectively, we arrive at

$$\frac{d\sigma_{\mu'}}{d\Omega} = (2S_0 + 1)\frac{\omega'}{2c} \int \sum_{l_am_a\mu_a} \sum_{l_bm_b\mu_b} \sum_{m'_am'_b} \mathcal{D}^{l^*_a}_{m'_am_a} \mathcal{D}^{l_b}_{m'_bm_b} \mathcal{D}^1_{\mu_a\mu'}$$
$$\mathcal{D}^{1^*}_{\mu_b\mu'} Y^*_{l_am'_a} Y_{l_bm'_b}$$
$$\langle\Psi_0|\hat{d}_{\mu_a}|\Psi^-_{\alpha\sigma l_am_aE}\rangle\langle\Psi^-_{\alpha\sigma l_bm_bE}|\hat{d}_{\mu_b}|\Psi_0\rangle \tag{18}$$

where primes refer to the laboratory frame. After exploiting the properties of Wigner matrices[38] to simplify the expression and using eq 15, the expression for β is found to be

$$\beta = -5\sqrt{\frac{2}{5}}\frac{F_2}{F_0} \tag{19}$$

where

$$F_J = \sum_{l_a,m_a,\mu_a} \sum_{l_b,m_b,\mu_b} \delta_{\mu_a+m_a,\mu_b+m_b}(-1)^J\langle l_b, J, l_a|0, 0\rangle$$
$$\langle l_a, J, l_b|m_a, m_b - m_a\rangle\langle 1, J, 1|\mu_b, \mu_a - \mu_b\rangle$$
$$i^{l_a-l_b} e^{i(\sigma_{l_b}-\sigma_{l_a})}\langle\Psi^-_{\alpha l_am_aE}|\hat{d}_{\mu_a}|\Psi_0\rangle^*\langle\Psi^-_{\alpha l_bm_bE}|\hat{d}_{\mu_b}|\Psi_0\rangle \tag{20}$$

Finally, $\langle\Psi^-_{\alpha lmE}|\hat{d}_{\mu_p}|\Psi_0\rangle$ can be expressed as a function of the real spherical harmonics (eq 6) and the Cartesian dipole operators (eq 11) whose integrals XCHEM computes

$$\langle\Psi^-_{\alpha lmE}|\hat{d}_{\mu_p}|\Psi_0\rangle = \left(1 - |\mu_p| + \frac{|\mu_p|}{\sqrt{2}}\right)\frac{a_m}{\sqrt{2}}$$
$$[-\mu_p\langle\Psi_0|\hat{d}_x|\Psi^-_{\alpha XlmE}\rangle - i\mu_p b_m\langle\Psi_0|\hat{d}_x|\Psi^-_{\alpha Xl-mE}\rangle$$
$$-i|\mu_p|\langle\Psi_0|\hat{d}_y|\Psi^-_{\alpha XlmE}\rangle + |\mu_p|b_m\langle\Psi_0|\hat{d}_y|\Psi^-_{\alpha Xl-mE}\rangle$$
$$+(1-|\mu_p|)\langle\Psi_0|\hat{d}_z|\Psi^-_{\alpha XlmE}\rangle$$
$$+ib_m(1-|\mu_p|)\langle\Psi_0|\hat{d}_z|\Psi^-_{\alpha Xl-mE}\rangle] \tag{21}$$

3. COMPUTATIONAL DETAILS

In the present study, we assume a photoionization process that leaves the CO cation in the $X^2\Sigma^+$, $A^2\Pi$, and $B^2\Sigma^+$ states at the experimental equilibrium geometry (D(C−O) = 1.128323 Å).
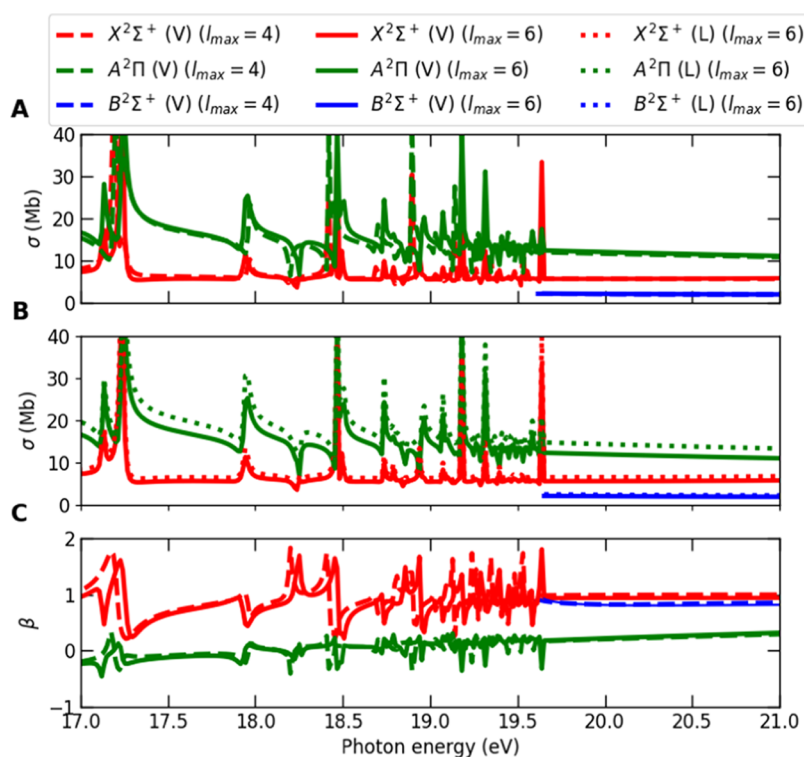
Figure 1. (A) Partial photoionization cross sections for $X^2\Sigma^+$ (red), $A^2\Pi$ (green), and $B^2\Sigma^+$ (blue) channels in the velocity gauge for the $l_{max} = 4$ and $l_{max} = 6$ calculations. (B) Same as (A) but comparing both gauges for the $l_{max} = 6$ calculation. (C) β asymmetry parameter (β) for $X^2\Sigma^+$ (red), $A^2\Pi$ (green), and $B^2\Sigma^+$ (blue) channels in the velocity gauge for the $l_{max} = 4$ and $l_{max} = 6$ calculations. Continuous lines correspond to the XCHEM calculation with $l_{max} = 4$ in the velocity gauge, dashed lines correspond to the XCHEM calculation with $l_{max} = 6$ in the velocity gauge, and dotted lines correspond to the XCHEM calculation with $l_{max} = 6$ in the length gauge.

The orbitals used in our calculations have been optimized by performing a restricted active space SCF (RASSCF) calculation for the ground state of the neutral molecule using a cc-pVQZ basis set and considering all configurations in which the 1σ and $1\sigma^*$ orbitals are doubly occupied; the 2σ, $2\sigma^*$, 3σ, $3\sigma^*$, 1π, and $1\pi^*$ orbitals can have an arbitrary number of electrons (complete active space) and the 4σ, $4\sigma^*$, 5σ, $5\sigma^*$, 6σ, $6\sigma^*$, 2π, $2\pi^*$ 3π, $3\pi^*$, 1δ, and $1\delta^*$ orbitals can have up to two electrons (restricted active space). These orbitals were then used to describe the $X^2\Sigma^+$, $A^2\Pi$, and $B^2\Sigma^+$ cationic states included in the close-coupling expansion (eq 1) by performing a similar RASSCF calculation. This approach yields a good description of the considered states as can be checked by comparing the calculated and the experimental ionization energies (experimental values indicated in parentheses), $X^2\Sigma^+$: 13.89 eV (14.0 eV), $A^2\Pi$: 16.94 eV (16.9 eV), and $B^2\Sigma^+$: 19.64 eV (19.7 eV).

The set of monocentric GABS used to describe the photoelectron is placed at the center of mass of the molecule. It consists of a set of 380 B-spline nodes of order 7 fixed between $R_{min} = 8.7$ au and $R_{max} = 200$ au, and a set of 22 even-tempered gaussian functions $G_i^M(r) \propto r^{2k+l}e^{-\alpha_i r^2}$, where $\alpha_i = \alpha_0 \beta^i$ ($\alpha_0 = 0.01$, $\beta = 1.46$, $i = 0, 1, ..., 21$), and the following combination of l and k values: $l = 0$, $k \leq 4$; $l = 1$, $k \leq 3$; $l = 2$, $k \leq 3$; $l = 3$, $k \leq 2$; $l = 4$, $k \leq 2$; $l = 5$, $k \leq 1$; $l = 6$, $k \leq 1$. From here on, we will refer to this XCHEM calculation as the $l_{max} = 6$ one.

4. RESULTS

In this work, we are interested in the energy region immediately below the $A^2\Pi$ and $B^2\Sigma^+$ cationic thresholds, where series of Rydberg states converge giving rise to several prominent resonances. The effect of including higher ionization thresholds (up to a photon energy of ∼30 eV) was checked by performing calculations with a smaller basis set. For this basis set, the cross sections obtained by including $X^2\Sigma^+$, $A^2\Pi$, and $B^2\Sigma^+$ channels and those obtained by including all open channels up to a photon energy of 30 eV were similar in the region below the third ionization threshold. Above this threshold, additional Feshbach resonances were found, and for this reason, we will not discuss such resonances in the present manuscript. Performing the same convergence test for the large basis set used in the manuscript is computationally very demanding. For this reason, we also computed the norms of the Dyson orbitals associated with the different ionization channels up to ∼35 eV. This was done using the RASSI module of OpenMolcas.[39] The Dyson orbital is defined as

$$\phi_{fi} = \sqrt{N} \int \Psi_f^{N-1}(x_2, x_3, ..., x_n)\Psi_i^N(x_1, x_2, ..., x_n)dx_2$$

$$... dx_N \tag{22}$$

where Ψ_i^N is the ground state of the molecule and Ψ_f^{N-1} is the electronic state of the molecular cation associated with channel f. By multiplying the above expression with the dipole operator and a one-electron continuum wave function, one obtains an approximation to the photoionization amplitude (static-exchange approximation). Although we have not used this approximation in our calculations, it can be used to
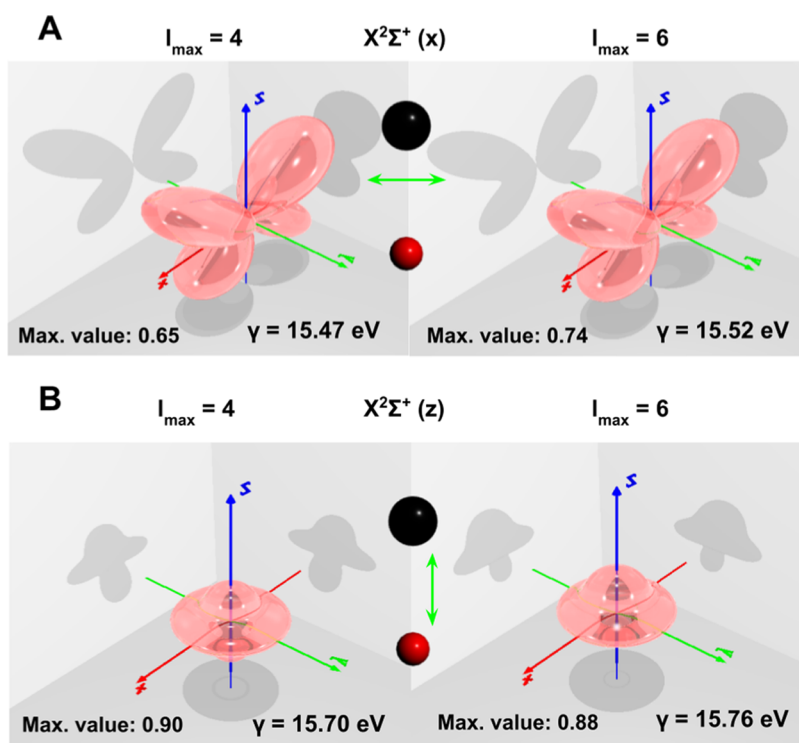
Figure 2. Comparison between MFPADs obtained from two different XCHEM calculations: with $l_{max} = 4$ (left) and $l_{max} = 6$ (right). For the sake of clarity, the MFPAD plots are normalized; the absolute value at the maximum is given in the labels. (A) MFPADs corresponding to transitions with photon energies $\gamma = 15.47$ and $\gamma = 15.52$ that populate a resonance in the $X^2\Sigma^2$ channel. The electric filed ($\vec{E}_{field}$) is polarized in the x direction. (B) MFPADs corresponding to transitions with photon energies ($\gamma = 15.70$ and $\gamma = 15.76$ respectively) that populate a resonance in the $X^2\Sigma^2$ channel. The electric filed ($\vec{E}_{field}$) is polarized in the z direction.

qualitatively analyze the relative importance of the different ionization channels. In particular, when the norm of eq 22 is very small for a given ionization channel f, one can safely conclude that the corresponding photoionization cross section will also be very small. We found that larger norms, close to 0.9, correspond to the three ionization channels included in our close-coupling calculations, which are mainly associated with one-hole states. Other ionization channels appearing above 23 eV, corresponding mainly to satellite states (or shake up states), have very small Dyson norms. As the values of these norms do not exceed 0.1, we can conclude that inclusion of these channels in the close-coupling expansion should not have a significant effect.

To check the convergence with angular momentum, we compare in Figure 1 the partial photoionization cross sections and the corresponding β asymmetry parameters, in velocity gauge, obtained with $l_{max} = 6$ with those resulting from another calculation with less angular flexibility ($l_{max} = 4$ and $k \leq 2$) and a similar but smaller RAS. The series of Rydberg states converging to the $B^2\Sigma^+$ threshold leads to Feshbach resonances in the electronic continuum of $X^2\Sigma^+$ and $A^2\Pi$ states. Since our calculation does not include any channel above the $B^2\Sigma^+$ threshold, no more resonances are expected above it. For both observables, the two basis sets lead to almost identical results in the whole energy region, suggesting that the $l_{max} = 6$ calculations are converged. This conclusion is further supported by the very good agreement between length and velocity results in the latter calculation.

As can be seen in Figure 1, resonances are associated with asymmetric peaks in the cross sections and to abrupt jumps in the β parameter at about the same energies. Consequently,

close to Feshbach resonances, abrupt changes in the MFPAD are also expected. Therefore, to ensure convergence of the MFPADs at the resonances, we compare the results of the two calculations described in the above paragraph in the vicinity of two resonances ($E_\gamma = 15.47$ eV and $E_\gamma = 15.70$ eV) appearing in the $X^2\Sigma^+$ channel for x and z laser polarizations, respectively (Figure 2). The results of both sets of calculations are in excellent agreement with each other, showing that convergence in the MFPADs is reasonably achieved in the $l_{max} = 6$ calculation.

Experimental partial cross sections are only available at higher photon energies,[17,40,41] where they do not have sufficient resolution to resolve any clear resonant feature. We have extended our calculations to these higher photon energies and compared with the experimental results, as shown in Figure 3. As can be seen, the agreement is quite reasonable, in spite of the fact that our calculations were designed to describe photoionization at much lower energies and only include three ionization channels. The relative difference between velocity and length gauges at these higher energies suggests that the residual discrepancy between experiment and theory may be due to the incomplete convergence of the close-coupling expansion in that energy region, which is largely expected since many of the channels that open there are not included in the calculation.

Figure 4 shows a comparison between our calculated partial cross sections in the velocity gauge with the available theoretical values[42−47] in the same energy region. A notable difference with our results is the absence of Feshbach resonances in all previously reported calculations, except for a few resonances predicted by the MCSCI method.[47] At higher
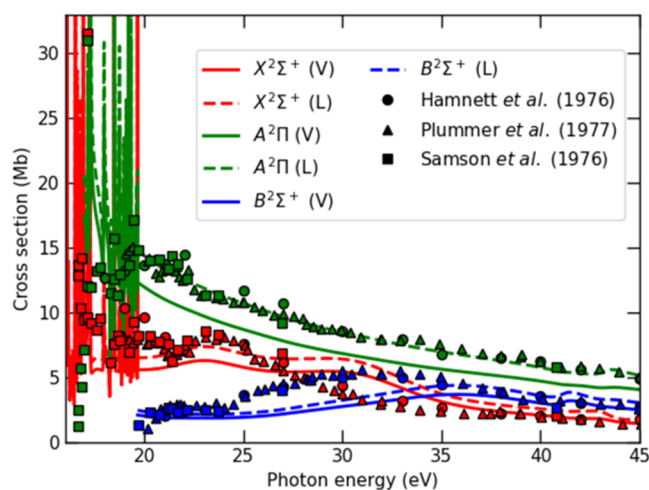
Figure 3. Partial photoionization cross sections for $X^2\Sigma^+$ (red), $A^2\Pi$ (green), and $B^2\Sigma^+$ (blue) cationic states. Continuous lines correspond to the XCHEM calculation with the velocity gauge, while dashed lines correspond to the XCHEM calculation with the length gauge. Experimental data obtained from (circles),[40] (triangles),[41] and (squares).[17]
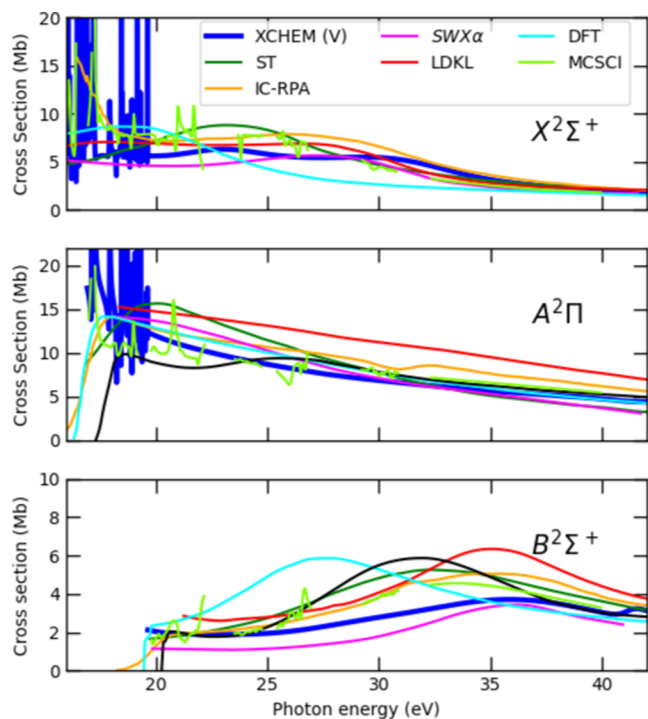
Figure 4. Partial photoionization cross sections for $X^2\Sigma^+$, $A^2\Pi$, and $B^2\Sigma^+$ channels. XCHEM results (in the velocity gauge) are presented among other theoretical calculations, namely, the scattered-wave $X\alpha$ method (STXα),[42] separated channel random-phase approximation (SC-RPA),[43] interacting channel random-phase approximation (IC-RPA),[43] Kohn variational principle Lobatto technique (LDKL),[44] Stieltjes−Tchebycheff (ST),[46] static-exchange DFT,[45] static-exchange time-dependent DFT (TDDFT),[45] and multichannel Schwinger configuration interaction method (MCSCI).[47]

energies, the XCHEM results are compatible with those of other calculations. These results support the notion that our description of the nonresonant part of the electronic continuum is reliable also in the region where Feshbach resonances appear.

In Figure 5, we compare our calculated MFPADs with those previously obtained by Lucchese[48] at 33 eV (photon energy) for the ionization channels leading to $X^2\Sigma^+$, $A^2\Pi$ and $B^2\Sigma^+$ cationic states and for the cases of alignment and antialignment of the laser polarization with respect to the molecular axis. The MFPADs are shown as a function of the angle between the laser polarization axis and the photoelectron direction, averaged over the two possible relative orientations of the carbon and oxygen atoms along the fixed molecular axis. The agreement is excellent for both gauges in all of the cases. The same is true in a wide range of photon energies above 16 eV, indicating that XCHEM is able to describe MFPADs at the same level of accuracy as the MCSCI method. At lower energies, where Feshbach resonances are present, some discrepancies are observed, which are likely due to the difference of the resonance positions in the two calculations.

In Figure 6, we compare the calculated β asymmetry parameters in the velocity gauge with the available experimental results.[49] Again, experimental data are only available in the higher photon energy region. For $X^2\Sigma^+$ and $A^2\Pi$ channels, the agreement with the experiment is quite good. For the $B^2\Sigma^+$ channel, a significant discrepancy with experiment can be seen up to ~30 eV. This could be explained by the missing higher ionization thresholds in our close-coupling expansion, which will mainly affect the highest ionization channel included in the calculations. As explained above, higher ionization channels were excluded from our calculations because they are not expected to contribute in the resonant region we are interested in.

5. DISCUSSION

We discuss now in more detail the effect of Feshbach resonances in the MFPADs at lower photon energies. Figures 7 and 8 show the variation of the MFPADs with photon energy for a cut along the xz plane (the molecular axis coincides with the z axis) and for $X^2\Sigma^+$ and $A^2\Pi$ channels. In the xz plane, the azimuthal angle is fixed ($\phi = 0$), so that all angular variations in the electron emission (in the molecular frame) are described by the polar angle θ (see balls' schemes in the figures). Figure 7 considers the case of laser polarization along the x direction, i.e., perpendicular to the molecular axis, whereas Figure 8 considers polarization along the z direction, i.e., parallel to the molecular axis. To guide the eye, the cross sections for the two different laser polarization directions have been included in the left margin of the figures. Figure 7 shows that, far from the resonance peaks, the electron angular distributions are almost the same for all photon energies in a given ionization channel. In the case of the $X^2\Sigma^+$ channel, the electron is preferentially ejected at 90°, i.e., electrons mainly follow the external electric field and escape perpendicularly to the molecular axis. In the case of the $A^2\Pi$ channel, the principal direction of ejection is still 90°, although there is also significant electron emission at around 0 and 180°. The latter is the consequence of the noncylindrical symmetry of the $A^2\Pi$ state in which the CO$^+$ ion is left. This picture changes completely in the vicinity of Feshbach resonances. In the $X^2\Sigma^+$ channel, the presence of the resonances favors electron emission toward either the carbon or the oxygen atoms, i.e., at 0 and 180°, depending on the particular resonance that one focuses on, while in the $A^2\Pi$ channel, electron emission is even more involved than in the absence of any resonance.

When the polarization direction of the incident light is parallel to the molecular axis (see Figure 8), near-threshold
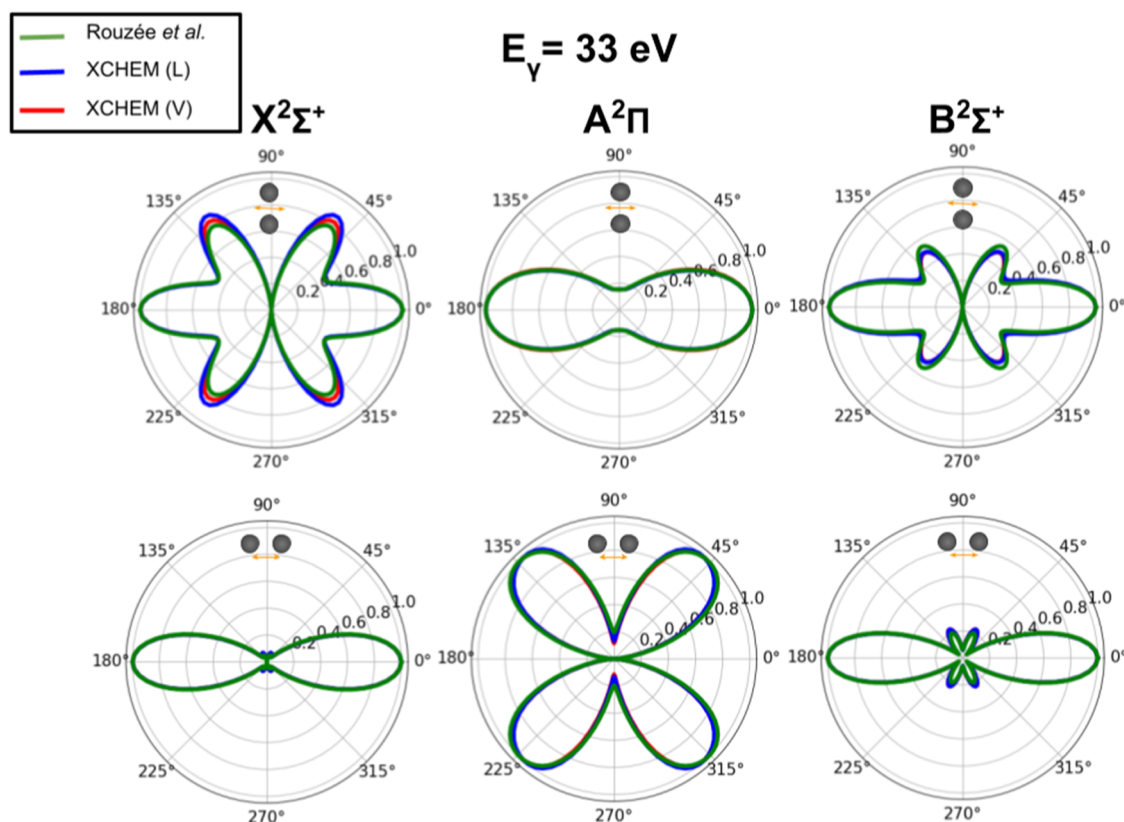
Figure 5. Normalized MFPADs obtained with XCHEM in velocity (red) and length (blue) gauges and with the MCSI approach of Lucchese et al.[48] at 33 eV (photon energy) for the ionization channels leading to $X^2\Sigma^+$, $A^2\Pi$ and $B^2\Sigma^+$ cationic states and for the cases of alignment (bottom) and antialignment (top). The MFPADs are represented as a function of the angle between the laser polarization direction and the direction of ejection of the photoelectron and averaging between both possible molecule orientations.
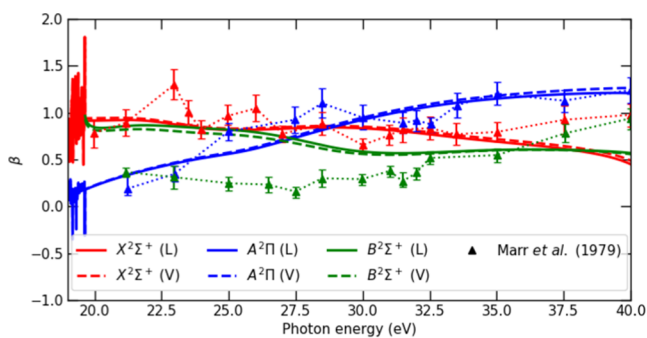

Figure 6. β asymmetry parameter (β) for $X^2\Sigma^+$ (red), $A^2\Pi$ (green), and $B^2\Sigma^+$ (blue) ionization channels. Continuous lines correspond to the XCHEM calculation in the velocity gauge, dashed lines in the length gauge, and triangles to the experimental data from Marr et al.[49]

photoelectrons in the $X^2\Sigma^+$ channel are mainly ejected toward the carbon atom, as can be clearly observed close to 14 eV. As we move to higher photon energies, still in the nonresonant regions, ejection around 110 and 180° starts to appear. This picture is again disrupted by the presence of the resonances. For example, the first resonance appearing at 14.4 eV favors electron emission toward the opposite direction, the oxygen atom. In the $A^2\Pi$ case, the preferred electron emission directions in the nonresonant regions are 45 and 135°. The presence of resonances modifies the relative intensities in these two directions.

The abrupt changes in the electron emission direction in the presence of resonances are the consequences of similarly

abrupt changes in the electron density. To illustrate this point in an intuitive way, we fix our attention to the resonance appearing at 14.4 eV in Figure 8, which significantly modifies the photoelectron direction toward the oxygen atom. Direct electron ejection into the continuum associated with the $X^2\Sigma^+$ channel can be easily understood by looking at the Dyson orbital resulting from the overlap between the ground state of CO and the $X^2\Sigma^+$ state of CO$^+$. This is shown in Figure 9A. The Dyson orbital is mainly located around the carbon atom, thus explaining why this is the preferred electron emission direction just below and above the resonance in question. At the resonance energy, two different paths to the continuum interfere: the direct ionization path just described and autoionization from the Feshbach resonance populated at this energy. This Feshbach resonance is a Rydberg state associated with the $A^2\Pi$ channel, which is embedded in the $X^2\Sigma^+$ continuum. The dominant electronic configurations can be respectively written as $1\sigma^2 1\sigma^{*2} 2\sigma^2 2\sigma^{*1} 1\pi^3 3\sigma^2 n\pi^1$ (Rydberg state) and $1\sigma^2 1\sigma^{*2} 2\sigma^2 2\sigma^{*1} 1\pi^4 3\sigma^1 \epsilon\sigma^1$ ($X^2\Sigma^+$ continuum). Therefore, the decay of the metastable Rydberg state to the continuum is a two-electron process in which one electron has to jump to the continuum and the other one has to move to a different bound orbital. In other words, a first electron must leave the diffuse Rydberg orbital $n\pi$ and a second one the 3σ orbital to end up in the 1π orbital and the continuum orbital $\epsilon\sigma$. Figure 9D shows the diffuse orbital $n\pi$ associated with the dominant configuration in the Rydberg state (for simplicity, only one of the two degenerate diffuse orbitals is shown) and Figure 9B,C the 3σ and 1π orbitals, respectively. These orbitals correspond to the dominant configurations in the multi-
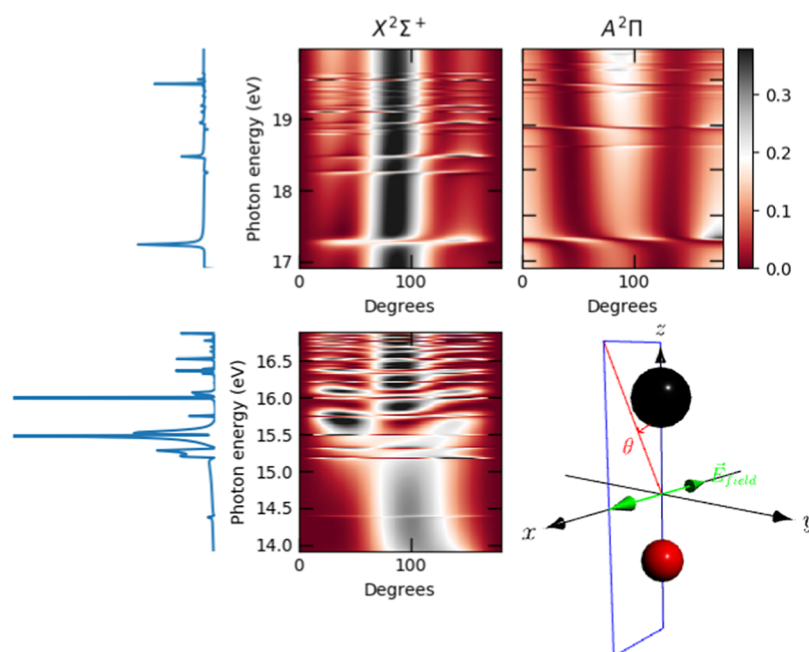
Figure 7. Cuts of the MFPADs through a plane that contains the molecular axis (xz plane, i.e., $\phi = 0$) as a function of photon energy for $X^2\Sigma^+$ and $A^2\Pi$ state channels. The electric field ($\vec{E}_{\text{field}}$) is polarized along the x direction (perpendicular to the molecular axis). See scheme in the bottom right. The corresponding cross sections are depicted on the left-hand side of the figure.
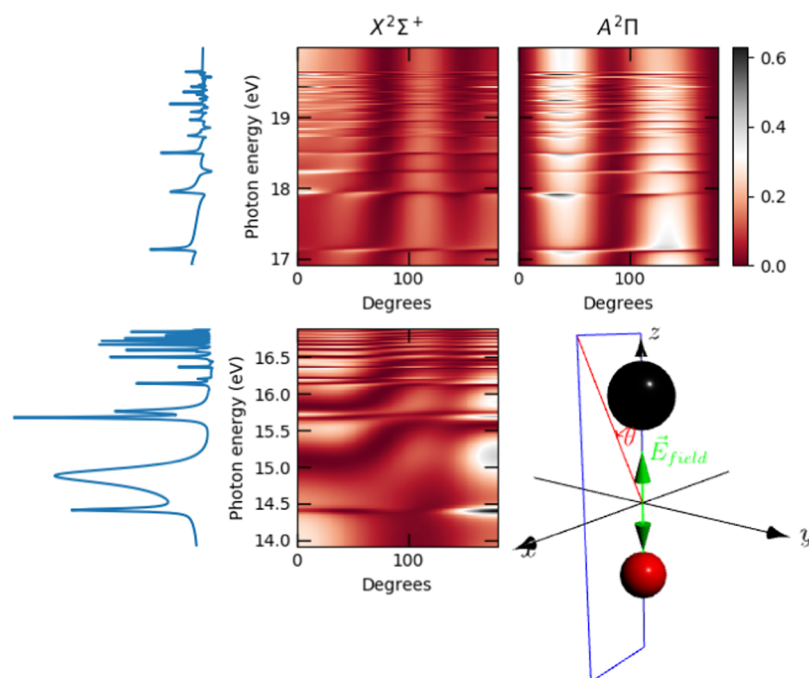

Figure 8. Same as Figure 7 when the electric filed ($\vec{E}_{\text{field}}$) is polarized along the z direction (parallel to the molecular axis).

reference expansion of the wave function. As the electrons are indistinguishable, one cannot know which electron goes where, but it can be clearly seen that all of the relevant orbitals in the autoionizing decay of the Feshbach resonance, namely, the initial Rydberg orbital (Figure 9D), the initial 3σ orbital (Figure 9C), and the final π orbital (Figure 9B) are mostly concentrated around the oxygen atom, thus explaining why electron emission is favored in this direction in contrast with the case in which no resonance is populated.

The results of Figure 9 show that Dyson orbitals, though potentially useful to qualitatively predict the preferential emission direction of the electron in a direct (nonresonant) ionization process, they are not appropriate for similar predictions in the region where Feshbach resonances appear. This is due to the important role played by correlation between the remaining electrons and the ionized ones in these regions, which cannot be accounted for by Dyson orbitals, since, by definition, the scaping electron is ignored (see eq 22).
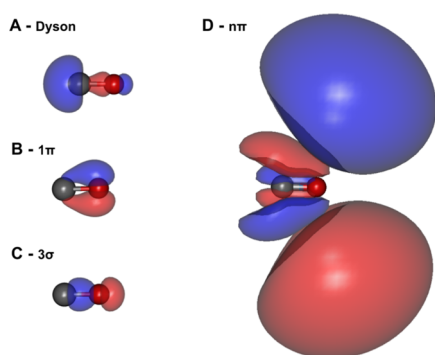
Figure 9. Orbitals involved in the resonant and nonresonant ionization pathways corresponding to the $X^2\Sigma^+$ channel. (A) Dyson orbital corresponding to the overlap between the ground state of CO and the $X^2\Sigma^+$ state of CO^+. (B) 1π orbital containing the unpaired electron in the dominant configuration of the $A^2\Pi$ cationic state. (C) 3σ orbital containing the unpaired electron in the dominant configuration of the $X^2\Sigma^+$ cationic state. (D) Rydberg orbital associated with the $A^2\Pi$ channel. For all orbitals, the isosurface corresponds to 70% of the orbital.

6. CONCLUSIONS

We have presented an extension of the XCHEM methodology to evaluate laboratory- and molecular-frame photoelectron angular distributions of molecules from accurate correlated electronic continuum wave functions. The method is particularly suitable to obtain photoelectron angular distributions in the region of the spectrum where strong correlation effects, as those associated with the decay of Feshbach resonances or with shake-up process, are important. The performance of the method has been demonstrated in the CO molecule, for which information on Feshbach resonances is very scarce. We have shown that, in the absence of any resonance, the calculated MFPADs are at least as accurate as those provided by other multireference methods to describe the ionization continuum of molecules. Our new results in the region where Feshbach resonances are present show that photoelectron angular distributions are dramatically affected by the presence of resonances, to the point that they can reverse the preferred electron emission direction. We have demonstrated that this pronounced effect is the consequence of important changes in the electronic structure of the molecule when resonances are populated, an effect that is mostly driven by electron correlation in the ionization continuum. We trust that the present methodology will help understand the measurement of angularly resolved photoionization time delays in this and more complex molecules.

AUTHOR INFORMATION

Corresponding Author

Fernando Martín − *Departamento de Química, Universidad Autónoma de Madrid, 28049 Madrid, Spain; Instituto Madrileño de Estudios Avanzados en Nanociencia (IMDEA-Nanociencia), 28049 Madrid, Spain; Condensed Matter Physics Center (IFIMAC), Universidad Autónoma de Madrid, 28049 Madrid, Spain;* ⊙ orcid.org/0000-0002-7529-925X; Email: fernando.martin@uam.es

Authors

Vicent J. Borràs − *Departamento de Química, Universidad Autónoma de Madrid, 28049 Madrid, Spain;* ⊙ orcid.org/0000-0002-4728-4042

Jesús González-Vázquez − *Departamento de Química, Universidad Autónoma de Madrid, 28049 Madrid, Spain;* ⊙ orcid.org/0000-0003-2204-3549

Luca Argenti − *Department of Physics and CREOL, University of Central Florida, Orlando, Florida 32186, United States*

Complete contact information is available at:
https://pubs.acs.org/10.1021/acs.jctc.1c00480

Notes
The authors declare no competing financial interest.

REFERENCES

(1) Svensson, S.; Eriksson, B.; Mårtensson, N.; Wendin, G.; Gelius, U. *J. Electron Spectrosc. Relat. Phenom.* **1988**, *47*, 327−384.

(2) Cirelli, C.; Marante, C.; Heuser, S.; Petersson, C. L. M.; Galán, J.; Argenti, L.; Zhong, S.; Busto, D.; Isinger, M.; Nandi, S.; Maclot, S.; Rading, L.; Johnsson, P.; Gisselbrecht, M.; Lucchini, M.; Gallmann, L.; Dahlström, J. M.; Lindroth, E.; L'Huillier, A.; Martín, F.; Keller, U. *Nat. Commun.* **2018**, *9*, No. 955.

(3) Heuser, S.; Jiménez Galán; Cirelli, C.; Marante, C.; Sabbar, M.; Boge, R.; Lucchini, M.; Gallmann, L.; Ivanov, I.; Kheifets, A. S.; Dahlström, J. M.; Lindroth, E.; Argenti, L.; Martín, F.; Keller, U. *Phys. Rev. A* **2016**, *94*, No. 063409.

(4) Vos, J.; Cattaneo, L.; Patchkovskii, S.; Zimmermann, T.; Cirelli, C.; Lucchini, M.; Kheifets, A.; Landsman, A. S.; Keller, U. *Science* **2018**, *360*, 1326−1330.

(5) Hockett, P. *J. Phys. B* **2017**, *50*, No. 154002.

(6) Hockett, P.; Frumker, E.; Villeneuve, D. M.; Corkum, P. B. *J. Phys. B* **2016**, *49*, No. 095602.

(7) Argenti, L.; Galán, J.; Taïeb, R.; Caillat, J.; Maquet, A.; Martín, F. *J. Phys.: Conf. Ser.* **2017**, *875*, No. 022040.

(8) Kotur, M.; Guénot, D.; Jiménez-Galán; Kroon, D.; Larsen, E. W.; Louisy, M.; Bengtsson, S.; Miranda, M.; Mauritsson, J.; Arnold, C. L.; Canton, S. E.; Gisselbrecht, M.; Carette, T.; Dahlström, J. M.; Lindroth, E.; Maquet, A.; Argenti, L.; Martín, F.; L'Huillier, A. *Nat. Commun.* **2016**, *7*, No. 10566.

(9) Dörner, R.; Mergel, V.; Jagutzki, O.; Spielberger, L.; Ullrich, J.; Moshammer, R.; Schmidt-Böcking, H. *Phys. Rep.* **2000**, *330*, 95−192.

(10) Cattaneo, L.; Vos, J.; Bello, R. Y.; Palacios, A.; Heuser, S.; Pedrelli, L.; Lucchini, M.; Cirelli, C.; Martín, F.; Keller, U. *Nat. Phys.* **2018**, *14*, 733−738.

(11) Jordan, I.; Huppert, M.; Rattenbacher, D.; Peper, M.; Jelovina, D.; Perry, C.; Conta, Av.; Schild, A.; Wörner, H. J. *Science* **2020**, *369*, 974−979.

(12) Klinker, M.; Marante, C.; Argenti, L.; González-Vázquez, J.; Martín, F. *J. Phys. Chem. Lett.* **2018**, *9*, 756−762.

(13) Dehmer, P. M.; Miller, P. J.; Chupka, W. A. *J. Chem. Phys.* **1984**, *80*, 1030−1038.

(14) Huber, K. P.; Stark, G.; Ito, K. *J. Chem. Phys.* **1993**, *98*, 4471−4477.

(15) Klinker, M.; Marante, C.; Argenti, L.; González-Vázquez, J.; Martín, F. *Phys. Rev. A* **2018**, *98*, No. 033413.

(16) Brion, C. E.; Tan, K. H.; van der Wiel, M. J.; van der Leeuw, P. E. *J. Electron Spectrosc. Relat. Phenom.* **1979**, *17*, 101−119.

(17) Samson, J. A. R.; Gardner, J. L. *J. Electron Spectrosc. Relat. Phenom.* **1976**, *8*, 35−44.

(18) Poullain, S. M.; Klinker, M.; González-Vázquez, J.; Martín, F. *Phys. Chem. Chem. Phys.* **2019**, *21*, 16497−16504.

(19) Carette, T.; Dahlström, J. M.; Argenti, L.; Lindroth, E. *Phys. Rev. A* **2013**, *87*, No. 023420.

(20) Berrington, K. A.; Eissner, W. B.; Norrington, P. H. *Comput. Phys. Commun.* **1995**, *92*, 290−420.

(21) Moore, L. R.; Lysaght, M. A.; Nikolopoulos, L. A. A.; Parker, J. S.; Hart, H. W. vd; Taylor, K. T. *J. Mod. Opt.* **2011**, *58*, 1132−1140.

(22) Carr, J. M.; Galiatsatos, P. G.; Gorfinkiel, J. D.; Harvey, A. G.; Lysaght, M. A.; Madden, D.; Mašín, Z.; Plummer, M.; Tennyson, J.; Varambhia, H. N. *Eur. Phys. J. D* **2012**, *66*, 58.

(23) Majety, V. P.; Scrinzi, A. *J. Phys. B* **2015**, *48*, No. 245603.

(24) Zielinski, A.; Majety, V. P.; Scrinzi, A. *Phys. Rev. A* **2016**, *93*, No. 023406.

(25) Lucchese, R. R.; Takatsuka, K.; McKoy, V. *Phys. Rep.* **1986**, *131*, 147−221.

(26) Stratmann, R. E.; Lucchese, R. R. *J. Chem. Phys.* **1995**, *102*, 8493−8505.

(27) Stratmann, R. E.; Zurales, R. W.; Lucchese, R. R. *J. Chem. Phys.* **1996**, *104*, 8989−9000.

(28) Lucchese, R. R.; Lafosse, A.; Brenot, J. C.; Guyon, P. M.; Houver, J. C.; Lebech, M.; Raseev, G.; Dowek, D. *Phys. Rev. A* **2002**, *65*, No. 020702.

(29) McCurdy, C. W.; Rescigno, T. N. *Phys. Rev. A* **1989**, *39*, 4487−4493.

(30) Schneider, B. I.; Rescigno, T. N.; McCurdy, C. W. *Phys. Rev. A* **1990**, *42*, 3132−3134.

(31) Rescigno, T. N.; Isaacs, W. A.; Orel, A. E.; Meyer, H.-D.; McCurdy, C. W. *Phys. Rev. A* **2002**, *65*, No. 032716.

(32) Jose, J.; Lucchese, R. R.; Rescigno, T. N. *J. Chem. Phys.* **2014**, *140*, No. 204305.

(33) Douguet, N.; Schneider, B. I.; Argenti, L. *Phys. Rev. A* **2018**, *98*, No. 023403.

(34) Marante, C.; Argenti, L.; Martín, F. *Phys. Rev. A* **2014**, *90*, No. 012506.

(35) Marante, C.; Klinker, M.; Corral, I.; González-Vázquez, J.; Argenti, L.; Martín, F. *J. Chem. Theory Comput.* **2017**, *13*, 499−514.

(36) Barreau, L.; Petersson, C. L. M.; Klinker, M.; Camper, A.; Marante, C.; Gorman, T.; Kiesewetter, D.; Argenti, L.; Agostini, P.; González-Vázquez, J.; Salières, P.; DiMauro, L. F.; Martín, F. *Phys. Rev. Lett.* **2019**, *122*, No. 253203.

(37) Reid, K. L. *Annu. Rev. Phys. Chem.* **2003**, *54*, 397−424.

(38) Varshalovich, D. A.; Moskalev, A. N.; Khersonskii, V. K. *Quantum Theory of Angular Momentum*; World Scientific: Singapore, 1988.

(39) Fdez Galván, I.; Vacher, M.; Alavi, A.; Angeli, C.; Aquilante, F.; Autschbach, J.; Bao, J. J.; Bokarev, S. I.; Bogdanov, N. A.; Carlson, R. K.; Chibotaru, L. F.; Creutzberg, J.; Dattani, N.; Delcey, M. G.; Dong, S. S.; Dreuw, A.; Freitag, L.; Frutos, L. M.; Gagliardi, L.; Gendron, F.; Giussani, A.; González, L.; Grell, G.; Guo, M.; Hoyer, C. E.; Johansson, M.; Keller, S.; Knecht, S.; Kovačević, G.; Källman, E.; Li Manni, G.; Lundberg, M.; Ma, Y.; Mai, S.; Malhado, J. P.; Malmqvist, P.; Marquetand, P.; Mewes, S. A.; Norell, J.; Olivucci, M.; Oppel, M.; Phung, Q. M.; Pierloot, K.; Plasser, F.; Reiher, M.; Sand, A. M.; Schapiro, I.; Sharma, P.; Stein, C. J.; Sørensen, L. K.; Truhlar, D. G.; Ugandi, M.; Ungur, L.; Valentini, A.; Vancoillie, S.; Veryazov, V.; Weser, O.; Wesołowski, T. A.; Widmark, P.-O.; Wouters, S.; Zech, A.; Zobel, J. P.; Lindh, R. *J. Chem. Theory Comput.* **2019**, *15*, 5925−5964.

(40) Hamnett, A.; Stoll, W.; Brion, C. E. *J. Electron Spectrosc. Relat. Phenom.* **1976**, *8*, 367−376.

(41) Plummer, E. W.; Gustafsson, T.; Gudat, W.; Eastman, D. E. *Phys. Rev. A* **1977**, *15*, 2339−2355.

(42) Davenport, J. W. *Phys. Rev. Lett.* **1976**, *36*, 945−949.

(43) Stener, M.; Decleva, P.; Cacelli, I.; Moccia, R.; Montuoro, R. *Chem. Phys.* **2001**, *272*, 15−25.

(44) Wilhelmy, I.; Ackermann, L.; Görling, A.; Rösch, N. *J. Chem. Phys.* **1994**, *100*, 2808−2820.

(45) Plésiat, E.; Decleva, P.; Martín, F. *Phys. Chem. Chem. Phys.* **2012**, *14*, 10853−10871.

(46) Padial, N.; Csanak, G.; McKoy, B. V.; Langhoff, P. W. *J. Chem. Phys.* **1978**, *69*, 2992−3004.

(47) Lebech, M.; Houver, J. C.; Raseev, G.; dos Santos, A. S.; Dowek, D.; Lucchese, R. R. *J. Chem. Phys.* **2012**, *136*, No. 094303.

(48) Rouzée, A.; Kelkensberg, F.; Kiu Siu, W.; Gademann, G.; Lucchese, R. R.; Vrakking, M. J. J. *J. Phys. B* **2012**, *45*, No. 074016.

(49) Marr, G. V.; Morton, J. M.; Holmes, R. M.; McCoy, D. G. *J. Phys. B* **1979**, *12*, 43−52.